Gas permeation effect on the Two-Section Two-Zone Fluidized Bed Membrane Reactor (TS-TZFBMR) fluid dynamics: a CFD simulation study

I. Julián, J. Herguido, M. Menéndez
Catalysis, Molecular Separations and Reactor Engineering Group (CREG), Aragon Institute of Engineering Research (I3A), Universidad de Zaragoza, Mariano Esquillor s/n, 50018 Zaragoza, Spain; tel. +34 876555168, e-mail: ijulian@unizar.es

Abstract

Two-Fluid Model simulations were conducted using the commercial software Ansys CFX and Fluent to study the effect of the gas extraction on the fluid dynamic behaviour of a Membrane-assisted Two-Section Two-Zone Fluidized Bed Reactor (TS-TZFBMR). Simulated bubble properties and bed dynamics were analyzed and compared among different membrane reactor configurations, including reactor-wall (RWM) and immersed tubular (ITM) membranes, for their future use in catalytic reactions, e.g. alkane dehydrogenation or methane steam reforming. According to the solids hold-up distribution at different fluidization regimes and permeation fluxes, the ITM configuration is the most suitable to enhance the gas-particle contact and to favor the solids axial mixing for in-situ catalyst regeneration purposes. However, the RWM configuration provides a greater permeation area for selective gas removal and is preferred to enhance purification. It was found that relative permeation fluxes above 20% of the total feed gas have a significant impact on the fluid dynamic regime within the TS-TZFBMR, concerning the appearance of local defluidized regions, gas channeling and solids axial mixing.

Keywords: Two-Fluid Model, Membrane reactor, Two-Zone Fluidized Bed Reactor, fluid dynamics, gas permeation

1. Introduction

The Two-Zone Fluidized Bed Reactor (TZFBR) represents an effective solution to counteract catalyst deactivation in gas-solid catalytic reactions affected by coking in the presence of light hydrocarbon feedstock [1, 2]. The TZFBR performance has been successfully tested for a number of processes including alkane dehydrogenation, steam reforming and aromatization [3-5] among others. All these processes involve a fast decay of catalytic activity due to catalyst fouling by coke deposition after some minutes on stream. Separated inlets for the gaseous reactants and the oxidizer (or regenerative agent) provide two different atmospheres along the bed. This configuration allows performing simultaneous catalytic reaction and catalyst regeneration in a single unit (Figure 1.a). According to previous studies [3, 6], the following variables may play a role on the process efficiency in a TZFBR: catalyst activity, selectivity and flowability, reaction temperature, fluidization regime, reactant-to-oxidizer ratio, reactive-to-regenerative bed volume ratio, arrangement of gas distributors or residence time, among

others. On this regard, the steady-state operation can only be achieved if the catalytic reaction and regeneration reaction rates as well as the solids axial mixing rate between bed zones are of the same order. For this reason, the understanding of the fluid dynamic behaviour of the reactor becomes essential to improve its design.

Recently, a conical transition section between bed zones with different cross-sectional area was implemented in order to get a better fluid dynamic control within each bed zone separately, resulting in the so-called Two-Section Two-Zone Fluidized Bed Reactor (TS-TZFBR) [5]. This novel configuration added basically three new operational variables to be considered in the reactor design: the tapered section angle, the relative distance between the axial position of secondary gas distributor inlet and the bottom-end of the conical bed section and the relative gas velocity within both reactor zones having different cross-sections. The authors characterized the fluid dynamic performance of the novel TS-TZFBR configuration by means of imaging techniques [7-9] and CFD simulations [10]. As a result, a novel bubble size correlation for the TS-TZFBR was proposed accounting for the effect of these three variables [7]. Additionally, the phenomenological Counter-Current Back-Mixing model (CCBM) [9] and the more detailed Two-Fluid Model (TFM) simulations [10] were validated against experimental tracers mixing and PIV/DIA (Particle Image Velocimetry & Digital Image Analysis) measurements on pseudo-2D TS-TZFBR [6, 8]. The study of this novel reactor fluid dynamics comprised lab scale beds of different sizes without and with several arrangements of internals in their lower zone [8].

A step further in the reactor design is the coupling of perm-selective membranes into the TS-TZFBR to reduce the downstream separation costs and capital costs, while improving the yield and selectivity of the process by overcoming the equilibrium conversion [11].

It is well known that membrane reactors combine the separation properties of membranes with the advantages of fluidized beds and represent a very promising technology in the field of process integration and intensification. Fluidized bed membrane reactors become especially attractive to generate ultra-pure hydrogen from water-gas-shift [12] or methane steam reforming [13-16]. These reactor configurations can also enhance the reactant conversion by H_2 removal as in alkane dehydrogenation [17].

It is obvious that the gas extraction from the catalytic bed shrinks the gas excess over minimum fluidization conditions and, thus, modifies the bubble properties and the overall bed dynamics. Therefore, the purpose of the present work is to study the effect of the membrane reactor configuration and the extent of gas extraction on the Two-Section Two-Zone Fluidized Bed Reactor (TS-TZFBMR) fluid dynamics in order to identify operational limitations and improve the multifunctional reactor design.

The main limitations of the membrane-assisted fluidized bed reactors are identified as the low hydrogen permeation rate through the perm-selective membranes and the eventual poor bubble-to-emulsion mass transfer derived from the gas extraction [14, 18, 19].

The first limitation can be overcome either by increasing the permeation area per reactor volume unit or by decreasing the membrane thickness and thereby increasing the permeability [11]. On the one hand, the reduction of the membrane thickness may compromise its stability

(lifetime) and perm-selectivity. On the other hand, the installation of a greater membrane surface may drastically reduce the space between membranes where the catalyst is suspended eventually leading to the concept of "micro-structured" fluidized bed membrane reactor [20]. This membrane reactor concept allows the bed to be operated at the turbulent fluidization regime at a relatively low gas velocity, thus improving mass transfer from the bubble to the emulsion phase and providing a gentler environment for the membranes [21].

The attenuation or possible removal of mass transfer limitations requires a deeper analysis on the solids hold-up distribution and bubble dynamics as a function of the membrane location, extraction degree and fluidization regime. In a first step towards a proper fluid dynamic design of a TS-TZFBMR, Two-Fluid Model (TFM) CFD simulations were conducted to investigate the effect of the membrane arrangement and permeated gas extent on the reactor dynamics.

Among the available simulation models to predict the complex fluid dynamic behaviour of multiphase flows [22], the Eulerian-Eulerian or Two-Fluid Model is preferred for the simulation of large gas-solid fluidized beds thanks to its reasonable compromise between accuracy and computational cost [23-25]. On this regard, several authors have recently used the Eulerian approach to describe the tapered bed dynamics [26, 27] as well as the hydrodynamic behaviour of fluidized beds with multiple jets [28] or with permselective membranes [29, 30].

However, this is the first time in which the simultaneous effect of multiple gas inlets, local gas extraction and a tapered region was evaluated for predicting the TS-TZFBMR fluid dynamics. As a first approach, the gas permeation was simulated as a fixed outward directed gas flux through the porous membrane walls of the computational domain. Two different membrane reactor arrangements were tested varying the membrane location with respect to the fluidized bed. The first configuration depicts the membrane as an immersed permeable tube located at the bed center within the upper reactor zone (Figure 1.b). In the second, certain region of the lateral reactor walls was set as permeable (Figure 1.c).

The Two-Fluid Model simulations were carried out using two commercial CFD codes: Ansys Fluent 12.1 and Ansys CFX 12.1. Fluent is one of the most inclusive software offered to the CFD community because of its wide range of industrial applications [31] and it is among the most widely employed software to perform gas-solid fluidized bed simulations. CFX was also used by a number of researchers [32, 33] to model the fluidized bed dynamics. Given that every CFD model involves several assumptions and needs to be validated against experimental results [34], the strengths and weaknesses in the predictability of both commercial codes were evaluated. For this purpose the fluid dynamic predictions of the different TFM formulations were compared to the experimental results obtained using Particle Image Velocimetry and Digital Image Analysis techniques [6] in similar reactors.

2. Computational model

2.1 Numerical model

The Eulerian model used to perform the computational simulations considers both solid and gas phase as interpenetrating continua, where the volume of a phase cannot be occupied

by others. Therefore, the concept of phase volume fraction is introduced. The model equations (eq. 1 to 3) consider mass and momentum conservation for each phase, *i* (gas or solid).

$$\frac{\partial}{\partial t}(\varepsilon_i \rho_i) + \nabla \cdot (\varepsilon_i \rho_i \vec{v}_i) = 0 \quad \text{(E.1)}$$

$$\frac{\partial}{\partial t}\left(\varepsilon_g \rho_g \vec{v}_g\right) + \nabla \cdot \left(\varepsilon_g \rho_g \vec{v}_g \vec{v}_g\right) = -\varepsilon_g \nabla P + \nabla \cdot \bar{\bar{\tau}}_g + \varepsilon_g \rho_g \vec{g} + K_{gs}(\vec{v}_g - \vec{v}_s) \quad \text{(E.2)}$$

$$\frac{\partial}{\partial t}(\varepsilon_s \rho_s \vec{v}_s) + \nabla \cdot (\varepsilon_s \rho_s \vec{v}_s \vec{v}_s) = -\varepsilon_s \nabla P - \nabla P_s + \nabla \cdot \bar{\bar{\tau}}_s + \varepsilon_s \rho_s \vec{g} + K_{gs}(\vec{v}_s - \vec{v}_g) \quad \text{(E.3)}$$

Essentially, both CFD codes employed in this work are suitable to simulate the TS-TZFBR fluid dynamics. Nevertheless, their spatial discretization methods (cell-centered for Fluent, vertex-centered for CFX), the available closure models and fluid dynamic parameters differ. For this reason, the choice of one or another depends on the required degree of detail, computational cost and numerical stability. On the one hand, the libraries of Fluent contain a greater number of models and parameters for the simulation of multiphase flows making this software more versatile. On the other hand, the CFX solver is faster and more stable [35, 36]. The model equations and discretization schemes used for Fluent and CFX are detailed below.

The left hand side of the momentum conservation equation represents the temporal and spatial transport terms. The right hand side represents the various interacting forces: buoyancy, pressure drop, viscous stress, gravity and interphase drag force. K_{gs} is the interphase momentum exchange coefficient whereas $\bar{\bar{\tau}}_i$ is the *i* phase stress-strain tensor.

The solution of this set of partial differential equations requires some closures to describe the interaction between phases. Concretely, the solid-fluid interphase momentum exchange coefficient was modeled with the Gidaspow drag function, that combines the equations of Ergun (equation 4) and Wen and Yu (equation 5) for the interphase drag force, where C_D was estimated using the Schiller-Naumann drag coefficient model (equation 6) and Re_s the particulate Reynolds number (equation 7). The interphase stress-strain tensor for the phase *i* (either gas or solid) was assumed to follow the Newtonian strain-rate relation, which depends on the bulk and shear viscosities (equation 8). Both the bulk (equation 9) and shear (equation 10) viscosities depend on the granular temperature (θ) and a collisional restitution coefficient (*e*). In this study, the restitution coefficient was set to *e* = 0.95. The angle of internal friction, φ, was set to 30º and the radial distribution function, g_0, (which measures the average distance between particles) was modeled according to the description of Lun and Savage [37]. To model the shear viscosity, Fluent uses the model of Gidaspow [38] to estimate the collisional (equation 11) and kinetic (equation 12) contributions plus the model of Schaefer [39] for the frictional viscosity (equation 13). However, Ansys CFX omits the frictional and kinetic contributions, thus calculating μ_s as the collisional viscosity given by the correlation of Gidaspow [38].

The granular temperature was determined algebraically under the assumption of local equilibrium in a transport equation model, i.e. energy production equals energy dissipation (equation 14), being the collisional dissipation of energy modeled according to the equation derived by Lun et al. [40] (equation 15). This assumption is often used in dense, slow moving fluidized beds where the local generation and dissipation of granular temperature far

outweigh the transport by convection and diffusion [41]. Lastly, the solids pressure was modeled according to the kinetic theory model of gases, being adapted to consider the inelastic collisions between particles (equation 16). The maximum solid packing, $\varepsilon_{s,m}$, was set to 0.65. A monodisperse 200 μm particle size distribution, which agrees with the particle size used in the experimental works, was used in the simulations throughout the study. The model parameters are listed in Table 1.

$$\varepsilon_g \leq 0.8 \;\rightarrow\; K_{gs} = 150\frac{\varepsilon_s(1-\varepsilon_g)\mu_g}{\varepsilon_g {d_p}^2} + 1.75\frac{\varepsilon_s \rho_g |\vec{v}_s - \vec{v}_g|}{d_p} \tag{E.4}$$

$$\varepsilon_g > 0.8 \;\rightarrow\; K_{gs} = \frac{3}{4} C_D \frac{\varepsilon_s \rho_g |\vec{v}_s - \vec{v}_g|}{d_p} {\varepsilon_g}^{-1.65} \tag{E.5}$$

$$C_D = \begin{cases} \frac{24}{\varepsilon_g Re_s}\left[1 + 0.15(\varepsilon_g Re_s)^{0.687}\right] & Re_s \leq 1000 \\ 0.44 & Re_s > 1000 \end{cases} \tag{E.6}$$

$$Re_s = \frac{d_p \rho_g |\vec{v}_s - \vec{v}_g|}{\mu_g} \tag{E.7}$$

$$\bar{\bar{\tau}}_i = \varepsilon_i \mu_i \left(\nabla \vec{v_i} + \nabla \vec{v_i}^T\right) + \varepsilon_i (\lambda_i - \frac{2}{3}\mu_i) \nabla \cdot \vec{v_i} \bar{\bar{I}} \tag{E.8}$$

$$\lambda_s = \frac{4}{3} {\varepsilon_s}^2 \rho_s d_p g_0 (1+e) \left(\frac{\theta}{\pi}\right)^{1/2} \tag{E.9}$$

$$\mu_s = \mu_{s,col} + \mu_{s,fr} + \mu_{s,kin} \tag{E.10}$$

$$\mu_{s,col} = \frac{4}{5} {\varepsilon_s}^2 \rho_s d_p g_0 (1+e) \left(\frac{\theta}{\pi}\right)^{1/2} \tag{E.11}$$

$$\mu_{s,kin} = \frac{5\rho_s d_p \sqrt{\theta\pi}}{48 g_0 (1+e)} \left[1 + \frac{4}{5} g_0 \varepsilon_s (1+e)\right]^2 \tag{E.12}$$

$$\mu_{s,fr} = \frac{P_s \sin\varphi}{2\sqrt{I_{2D}}} \tag{E.13}$$

$$\gamma_{\theta_s} = \left(-\nabla P_s \bar{\bar{I}} + \bar{\bar{\tau}}_s\right) : \nabla \vec{v}_s \tag{E.14}$$

$$\gamma_{\theta_s} = \frac{12(1-e^2) g_0}{d_p \sqrt{\pi}} \rho_s {\varepsilon_s}^2 \theta^{3/2} \tag{E.15}$$

$$P_s = \varepsilon_s \rho_s \theta \left(1 + 2\,\varepsilon_s g_0 (1+e)\right) \tag{E.16}$$

The set of governing equations was solved using a finite volume method for the different TS-TZFBR geometries depicted in Figure 1, dividing the computational domain into control

volumes. In Fluent, the pressure and velocity fields of the momentum equation were solved iteratively via a SIMPLE (*Semi Implicit Method for Pressure Linked Equations*) scheme. On the contrary, CFX uses a coupled solver to solve the transient mass and momentum equations as a single system. The convergence criterion for both codes was based on the residual error in the mass and momentum equations, which was set to 10^{-3}.

The numerical discretization of the model equations followed a first-order upwind scheme for the phase volumetric fractions and second-order upwind scheme for pressure and velocity fields. In Fluent, the cell-based spatial gradients were computed by the least-squares method. The discretization of the transient terms followed a first-order backward Euler (for improved numerical stability) in CFX, being second-order (for improved accuracy) in Fluent. An adaptive time step (10^{-4} – $2 \cdot 10^{-4}$ seconds) was used to achieve a faster convergence in Ansys CFX whereas a constant time step of 10^{-4} seconds was employed in Fluent simulations.

2.2 Computational domain

The TFM simulations were conducted in two different pseudo-2D membrane-assisted TS-TZFBR configurations. Membranes for gas extraction were located either surrounding the immersed gas distributor tube (Figure 1.b) or at the lateral reactor walls (Figure 1.c). The simulated reactor domain mimicked half of the depth-wise experimental bed geometry. The total dimensions of the computational domain were: 30 x 4 x 0.4 (height x width x depth, in cm). The tapered angle that connects the TS-TZFBR straight bed zones was α = 60º, with respect to the horizontal axis. The width of the lower bed zone was 2 cm and its height was 8 cm. The immersed T-shaped gas distributor orifices ($\varnothing_{orif}$ = 0.3 cm) were axially located at the bottom-end of the tapered bed region. Air was used as fluidization gas and the dense phase was described as a monodisperse distribution of spherical particles (d_p = 200 μm, ρ_{bulk} = 2.5 g/cm^3, $\varepsilon_{s,max}$ = 0.65, u_{mf} = 10.1 cm/s). Both simulated membranes were 6 centimeters high and their bottom-end was located at the upper straight bed zone, 2 centimeters above the tapered bed region. The reactor dimensions, detailed in Figure 1.a, mimic these used in previous experimental studies [6, 7, 9]. Mesh independence studies were conducted to find suitable conditions in terms of computational cost, numerical stability and reproducibility of hydrodynamic results. On this regard, the computational domain was finally discretized by more than 32000 hexahedra defining a structured mesh with an edge length in the range 0.10 – 0.12 cm (5 to 6 times the fluidized particle size).

2.3 Initial and boundary conditions

All simulations start off from a fixed bed with homogeneous solids volume fraction, being the same as the maximum bed packing measured experimentally.

A ‘bulk mass flow rate’ boundary condition was selected for the reactor gas inlets to avoid dense phase outflow. An ‘opening’ boundary was applied to the reactor outlet at the top of the domain. The opening condition refers to the unrestricted circulation of gas and dense phase (if it eventually reaches the top of the bed) through the boundary. The flow direction through inlets and outlets was defined as normal to the boundary surface.

At the reactor walls (front, rear and lateral bed walls, as well as the immersed T-shaped distributor wall) a fluid-dependant boundary was applied. The used no-slip condition for the gas phase is widely accepted and generally proposed. However, the proper selection of the particle-wall boundary condition is not so straightforward for Euler-Euler models and different formulations can be found in the open literature: no-slip [42], partial-slip [43-45] and free-slip [46, 47]. Although it seems that the partial-slip is the most realistic approach, the selection of an appropriated specularity coefficient is not trivial and needs to be done with care. In addition, some recent studies [48-50] suggest that the concept of a constant specularity coefficient proposed by Johnson and Jackson [51] is not generally applicable. Since the detailed analysis of the wall-particle friction is out of the scope of this work, a free-slip boundary condition was applied for the dense phase as a first approach.

Finally, a reverse 'bulk mass flow rate' boundary condition was applied to the simulated membranes. For simplicity the permeation rate was here described as the gas flow through the membranes, which represents a certain volumetric fraction of the total inlet gas flow.

2.4 Simulation case studies

Ten different operational conditions combining two inlet gas velocities (u_r = 1.5 and u_r = 2.5), two membrane configurations (ITM and RWM) and three permeation rates (0%, 20% and 50% with respect to the total inlet gas flow) have been tested to analyze the effect of gas permeation on the hydrodynamic performance of a TS-TZFBMR.

The selected relative gas velocities are in the range of the optimal u_r values obtained for alkane dehydrogenation in similar membrane-assisted TS-TZFBR facilities [3, 52]. On this regard, the simulated tapered angle was kept constant throughout the study ($\alpha = 60^o$) to mimic the reactor geometry used in these experimental studies.

On the contrary, the tested permeation rates are quite higher than these measured experimentally for H_2 removal through Pd-based membranes (~ 5%). The purposes of testing one order of magnitude greater permeation rates are: a) to enhance and make clear the effect (if any) of the gas removal on the TS-TZFBMR fluidization regime; b) to establish upper permeation limits for the applicability of previous hydrodynamic findings on membrane-assisted TS-TZFBR, e.g. the use of the JHM model for predicting the bubble size evolution [7].

3. Results

This section illustrates the main findings regarding the effect of the membrane-reactor arrangement, either ITM or RWM, and the permeation flux on the simulated TS-TZFBMR fluid dynamics. Bubble properties such as size and velocity profiles, radial distribution and aspect ratio will be analyzed and discussed. Analogously, transient average solids hold-up and axial velocity profiles will be compared in order to identify fluid dynamic limitations within the TS-TZFBMR. As a previous point, the ability of the commercial software CFX and Fluent to predict the experimental bubble characteristics and solids motion in a pseudo-2D TS-TZFBR without gas extraction will be tested.

Regarding the limitations and applicability of the following results to represent a real case where chemical reaction would take place, the bubble size distribution obtained in the simulations may be considered a good approach to that existing in chemical reactors if the change in the total molar flow because of the reaction is small. For example, reactions such as the selective oxidation of CO in the presence of a large concentration of hydrogen would imply a very low change in the total flow. In the same way, the steam reforming of methane, if performed with a large steam-to-carbon ratio would show only a small change in the total flow. On the contrary, the glycerol steam reforming with a small steam-to-carbon ratio ($C_3H_6O_3 + H_2O \rightarrow 2CO + CO_2 + 4H_2$) would imply a large increase of the molar flow, thus reducing the applicability of the presented fluid dynamic results.

3.1 Predictability of the experimental TS-TZFBR fluid dynamic behaviour

The simulated TS-TZFBR fluid dynamic results obtained by the commercial codes at several fluidization gas velocities were compared with the experimental PIV/DIA measurements from the authors in a previous study [6].

In Figure 2 the main experimental and simulated bubble characteristics obtained at relative gas velocities u_r = 1.5 and 2.5 are displayed. Figure 2.a illustrates the axial evolution of the equivalent bubble diameter whereas Figure 2.b shows the bubble size distribution at each regime. Both CFX and Fluent simulation results correspond to average bubble data over 8 seconds on stream while the experimental values were averaged out of 40 seconds on stream. Following the recommendations of some authors [24, 53-57], a solids volume fraction ε_s = 0.15 was used as a threshold value to identify bubble boundaries.

Although the variety of model closures and discretization schemes available in CFX is lower than in Fluent, the more unconstrained (and faster) TFM formulation used in CFX resulted in similar accuracy than that showed by Fluent to predict the experimental bubble characteristics. Concretely, the average relative error in the prediction of the experimental d_b along the bed height was: 8.8% and 11.2% for CFX and 4.8% and 8.7% for Fluent at u_r = 1.5 and 2.5, respectively. Due to the low discrepancies between the predictions of CFX and Fluent and the lower computational cost of the CFX code, CFX was selected to perform the statistical analysis on the simulated bubble hydrodynamics in a membrane-assisted TS-TZFBR, i.e. the TS-TZFBMR.

The model predictions of the experimental solids hold-up distribution and local solids motion are shown in Figure 3. Figure 3.a shows the axial evolution of the experimental and simulated solids volume fraction at two gas velocities. Figure 3.b illustrates the time-averaged solids velocity in the upward and downward directions along the vertical position in the bed measured at u_r = 2.5. In general, it is observed that CFX overestimates the experimental bed packing and, thus, predicts a lower fluidized bed height. On the contrary, Fluent underestimates the experimental solids hold-up along the bed at the different fluidization regimes, although it predicts both the total bed height and the axial evolution of the solids volume fraction qualitatively at the two gas velocities. The experimental solids motion depicts quasi-symmetric time-averaged upward and downward velocity profiles at u_r = 2.5. The axial solids velocity increases along the vertical axis within the straight bed zones whereas it

decreases within the tapered bed region, following the same trend as that observed for the average bubble size depicted in Figure 2.a. Fluent is able to predict the axial solids velocity profile along the whole bed while CFX clearly overestimates the upward and downward particle velocities (given in absolute values) within the upper bed zone, i.e. z = 10 – 15 cm. This suggests that the more relaxed constraints used in the CFX model formulation with respect to these used in Fluent lead to a poor estimation of the solids motion and hold-up distribution in a TS-TZFBR. For this reason, Fluent was selected as the simulation tool to evaluate the detailed bed fluid dynamics in a TS-TZFBMR.

3.2 TS-TZFBMR Bubble properties

The measurement of the axial evolution of the equivalent bubble diameter, $d_b(z)$, allows quantifying the average bubble size decrease as a function of the permeation rate and membrane location. Figure 4.a shows that, under the same relative fluidization gas velocity (u_r = 2.5), the RWM configuration leads to a sharper bubble size shrinkage along the permeable region in comparison to that for an ITM bed. This trend has been observed regardless the inlet gas velocity and the degree of gas extraction (Figures 4.b and 4.c). Even for the limiting case, in which the mean gas velocity in the upper bed region over the membrane is below the minimum fluidization velocity (u_r = 1.5 and 50% of the total gas permeated), small bubbles are still detected in the ITM configuration whereas no bubbles are measured in the RWM simulated bed.

The bubble size probability distribution measured for the TS-TZFBR and the membrane-assisted ITM and RWM configurations at u_r = 2.5 and 20% extraction (Figure 5.a) illustrates that the use of a RWM arrangement leads to a substantial bubble size shrinkage with respect to the ITM configuration under the same gas flow conditions. However, the classical bubble velocity correlation developed by Davidson and Harrison for straight fluidized beds gives a quite accurate prediction of the u_b evolution as a function of the bubble size within the TS-TZFBMR regardless the membrane configuration. Figure 5.b suggests that the multiple gas inlets, unconventional geometry and selective gas removal do not have a relevant impact on the $u_b(d_b^{0.5})$ function linearity. As a result, the membrane configuration that leads to the smallest bubbles leads analogously to the lowest solids axial mixing rates.

The discrepancy between the bubble size distribution profiles for ITM and RWM membrane-reactor configurations operating at same conditions motivated the study of further bubble properties such their radial distribution along the region of interest, i.e. the bed section affected by the membrane. The Figure 6 depicts the radial distribution of bubble centroids within different bed regions for TS-TZFBR and TS-TZFBMR (20% extraction) at u_r = 2.5. Figures 6.a to 6.c analyze the radial distribution within the bed region affected by the IT and RW membranes whereas Figures 6.d to 6.f illustrate the effect of the membrane configuration on the distribution of bubble centroids within the lower straight bed zone.

The tri-modal distribution of bubble centroids found in the upper bed region (Figures 6.a to 6.c) is caused by the three bubble sources acting at that height: the bubbles coming from the two orifices of the immersed gas distributor and those coming from the bottom distributor. In the case without gas extraction, the bubbles flow up basically through the bed center with a

marginal radial dispersion related to the bubbles coming from the immersed distributor. The use of an ITM broadens the distribution of bubble centroids in the vicinity of the bed center and reduces the relative probability of the central peak against the side peaks. In case of lateral extraction (RWM), bubbles tend to flow towards the wall-membranes thus increasing the radial dispersion. As a result, the probability of finding bubbles within the bed annulus becomes greater than that of finding them along the bed core.

It has been found that the effect of the membrane arrangement and gas extraction on the bubble radial distribution within the lower bed zone (Figures 6.d. to 6.f) is almost negligible. Nevertheless, it can be observed that the central location of the gas extraction in the ITM arrangement tends to promote an enhanced flow of bubbles through the bed center in that bed region in comparison to that for the TS-TZFBR or RWM.

3.3 TS-TZFBMR solids hold-up and velocity distribution maps

For the considered membrane-assisted TS-TZFBR configurations, i.e. ITM and RWM, the time-averaged (Δt = 8 s) dense phase porosity and axial velocity maps have been obtained using Fluent software. The purpose is to study the spatial solids hold-up, the dense phase dynamics and the porosity and velocity fluctuation along the time on stream in order to detect operational problems such as channeling or defluidization, as a function of the fluidization regime and extent of gas permeated.

Figure 7 shows the solids-hold up distribution for different gas extraction rates (0%, 20% and 50%) and membrane configurations (ITM and RWM) at a fluidization regime u_r = 2.5. The gas extraction induces for the RWM configuration a greater radial porosity gradient between the lateral walls and the bed center, leading to a lower bed expansion (greater packing) and an enhanced preferential path for the axial solids circulation through the bed center with respect to the ITM configuration. This finding, together with the previous results on the bubbling fluidization, confirms that the solid mixing is favored in the ITM membrane arrangement.

Although the RWM configuration allows greater permeation areas and, thus, enhanced extraction flow rates, this membrane arrangement would compromise the TS-TZFBMR mass and heat transfer requirements for the process integration. It has been shown that the RWM configuration worsens both the gas-solid contact (i.e. the catalytic conversion, when operating under reaction conditions) and the axial mixing (i.e. the in-situ catalyst regeneration, when operating under reaction conditions), while enhancing mass transfer limitations for the gas permeation as a result of the densely packed regions arose close to the reactor walls.

The analysis of the transient fluctuation of the bed properties, viz. local porosity and solids velocity, allowed the study of the defluidization or formation of dead-zones within the TS-TZFBMR tapered bed region. In this study the bed regions in which the time-averaged solids volume fraction (Figure 8.a) is greater than 0.62 and the axial velocity (Figure 8.c) is lower than 0.5 cm/s, being the porosity (Figure 8.b) and velocity fluctuation (Figure 8.d) lower than 0.05 and 0.03 cm/s respectively, are considered as banked or defluidized zones. Figure 8.e illustrates the defluidized zones detected on both sides of the tapered bed region for an ITM (20%) configuration at u_r = 2.5 as a convolution of the four previous restrictions. The so-called

defluidization angle, β, indicates the slope of the defluidized region boundaries with respect to the horizontal position as it is shown in Figure 8.e.

In previous studies [6, 7, 9, 10], a conservative tapered section angle α = 80^{o} was found as a suitable reactor wall inclination angle to avoid defluidization phenomena within a TS-TZFBR under every fluidization condition. However, the use of in-situ perm-selective membranes for gas removal (TS-TZFBMR) enhances defluidization and such conservative α value may be eventually exceeded at low fluidization regimes and high permeation rates, as it can be observed in Table 2.

4. Conclusions

Two commercial CFD codes, Fluent and CFX, were employed to simulate the effect of gas extraction and membrane arrangement on the TS-TZFBMR fluid dynamics. Fluent provided a substantially better prediction of the experimental solids motion and hold-up distribution. However, both codes were suitable to reproduce the experimental average bubble size profile qualitatively ($\sim$ 10% error in the worst scenario). According to the simulation results, the membrane arrangement does have an impact on the bubble characteristics: a 20% gas extraction rate reduced the average bubble size (within the bed region affected by the membrane) by 18% in the case of ITM and by 31% for the RWM configuration. The membrane location also affected the solids hold-up distribution: the RWM configuration led to densely packed regions and enhanced defluidization near the bed walls in comparison to that in the ITM arrangement.

Although the RWM configuration provides a greater permeation area for selective gas removal, the ITM arrangement favors the solids axial mixing, which in our case would be useful for process integration purposes. Therefore, a compromise between the permeation flow rates and the membrane location needs to be reached in order to optimize the reactor performance.

Acknowledgements

Financial support from MINECO, Spain (Projects CTQ2010-15568 and ENE2013-44350-R) is gratefully acknowledged. Financial aid for the maintenance of the consolidated research group CREG has been provided by the Fondo Social Europeo (FSE) through the Gobierno de Aragón (Aragón, Spain).

Nomenclature

C_D	Interphase drag coefficient, (-)
CFD	Computational Fluid Dynamics
d_b	Equivalent bubble diameter, (cm)
d_p	Particle diameter, (m)
DIA	Digital Image Analysis
e	Restitution coefficient, (-)
g	Acceleration due to gravity, (m s^{-2})

g_0	Radial distribution function, (-)
$\bar{\bar{I}}$	Stress tensor, (-)
ITM	Internal tubular membrane
I_{2D}	Second invariant of the deviatory stress tensor, (-)
K	Bubble velocity coefficient, (-)
K_{gs}	Interphase momentum exchange coefficient, (kg $m^{-3}s^{-1}$)
P	Pressure, (Pa)
PIV	Particle Image Velocimetry
Re	Reynolds number, (-)
RWM	Reactor-wall membrane
TS-TZFBR	Two-Section Two Zone Fluidized Bed Reactor
TS-TZFBMR	Two-Section Two Zone Fluidized Bed Membrane Reactor
TZFBR	Two-Zone Fluidized Bed Reactor
u_b	Single bubble velocity, (cm s^{-1})
u_{br}	Bubbles velocity, (cm s^{-1})
u_{gas}	Gas velocity, (cm s^{-1})
u_{mf}	Minimum fluidization velocity, (cm s^{-1})
$u_{r,bottom}$	Relative velocity (u_{gas}/u_{mf}) within the lower bed section, (-)
$u_{r,top}$	Relative velocity (u_{gas}/u_{mf}) within the upper bed section, (-)
$\vec{v}$	Local velocity, (m s^{-1})
y	Bed depth, (cm)
z_{dis}	Immersed distributor axial location, (cm)
z_{sc}	TS-TZFBR section change axial location, (cm)

Greek symbols

α	Tapered section angle, (^{o})
β	Defluidization angle, (^{o})
$\gamma_{\Theta s}$	Collision dissipation energy, (kg $m^{-1}s^{-3}$)
ε	Volume fraction, (-)
θ	Granular temperature, (m^2s^{-2})
λ	Bulk viscosity, (kg $m^{-1}s^{-1}$)
μ	Shear viscosity, (kg $m^{-1}s^{-1}$)
μ_{col}	Collisional shear viscosity, (kg $m^{-1}s^{-1}$)
μ_{kin}	Kinematic shear viscosity, (kg $m^{-1}s^{-1}$)
μ_{fr}	Frictional shear viscosity, (kg $m^{-1}s^{-1}$)
ρ	Density, (kg m^{-3})
$\bar{\bar{\tau}}$	Stress-strain tensor, (kg $m^{-1}s^{-2}$)
φ	Angle of internal friction in particle collisions, (^{o})
ω	Probability density of bubble size, (%)

Subscripts

i	Phase i, either fluid or solid
g	Fluid phase (gas)
s	Solid phase

m	maximum
0	initial

References

[1]. J. Herguido, M. Menéndez, J. Santamaría, On the use of fluidized bed catalytic reactors where reduction and oxidation zones are present simultaneously. Catal. Today. 100 (2005) 181-189.

[2] S. Parient, V. Belliere-Baca, S. Paul, N. Fatah, Process for obtaining acrolein by catalytic dehydration of glycerol or glycerin. US Patent: US 20130217909 A1 (2013)

[3]. J.A. Medrano, I. Julián, F. García-García, K. Li, J. Herguido, M. Menéndez, Two-Zone Fluidized Bed Reactor (TZFBR) with palladium membrane for catalytic propane dehydrogenation: experimental performance assessment. Ind. Eng. Chem. Res. 52 (2013) 3723-3731.

[4]. L. Pérez-Moreno, J. Soler, J. Herguido, M. Menéndez, Stable hydrogen production by methane steam reforming in a two-zone fluidized-bed reactor: Effect of the operating variables. Int. J. Hydrogen Energy. 38 (2013) 7830-7838.

[5]. M.P. Gimeno, J. Soler, J. Herguido, M. Menéndez, Counteracting catalyst deactivation in methane aromatization with a Two Zone Fluidized Bed Reactor. Ind. Eng. Chem. Res. 49 (2010) 996-1000.

[6]. I. Julián, F. Gallucci, M. van Sint Annaland, J. Herguido, M. Menéndez, Coupled PIV/DIA for fluid dynamics studies on a Two-Section Two-Zone Fluidized Bed Reactor. Chem. Eng. J. 207-208 (2012) 122-132.

[7]. I. Julián, J. Herguido, M. Menéndez, A non-parametric bubble size correlation for a Two-Section Two-Zone Fluidized Bed Reactor (TS-TZFBR). Powder Technol. 256 (2014) 146-157.

[8]. I. Julián, F. Gallucci, M. van Sint Annaland, J. Herguido, M. Menéndez, Hydrodynamic study of a Two-Section Two-Zone Fluidized Bed Reactor with an immersed tube bank via PIV/DIA. Chem. Eng. Sci. 134 (2015) 238-250.

[9]. I. Julián, J. Herguido, M. Menéndez, Particle mixing in a Two-Section Two-Zone Fluidized Bed Reactor. Experimental technique and Counter-Current Back-Mixing model validation. Ind. Eng. Chem. Res. 52 (2013) 13587-13596.

[10]. I. Julián, J. Herguido, M. Menéndez, CFD model prediction of the Two-Section Two-Zone Fluidized Bed Reactor (TS-TZFBR) hydrodynamics. Chem. Eng. J. 248 (2014) 352-362.

[11]. F. Gallucci, E. Fernandez, P. Corengia, M. van Sint Annaland, Recent advances on membranes and membrane reactors for hydrogen production. Chem. Eng. Sci. 92 (2013) 40-66.

[12]. A. Basile, L.A. Paturzo, F. Gallucci, Co-current and counter-current modes for water gas shift membrane reactor. Catal. Today. 82 (2003) 275-281.

[13]. A. Basile, F. Gallucci, L.A. Paturzo, dense Pd/Ag membrane reactor for methanol steam reforming: Experimental study. Catal. Today. 104 (2005) 244-250.

[14]. L. Tan, I. Roghair, M. van Sint Annaland, Simulation study on the effect of gas permeation on the hydrodynamic characteristics of membrane-assisted micro fluidized beds. Appl. Math. Model. 38 (2014) 4291-4307.

[15]. A. Adris, S. Elnashaie, R.A. Hughes, Fluidized-bed membrane reactor for the steam reforming of methane. Can. J. Chem. Eng. 69 (1991) 1061-1070.

[16]. F. Gallucci, M. van Sint Annaland, J.A.M. Kuipers, Autothermal reforming of methane with integrated CO_2 capture in a novel fluidized bed membrane reactor. Part 1: Experimental Demonstration. Top. Catal. 51 (2008) 133-145.

[17]. R. Dittmeyer, V. Höllein, K. Daub, Membrane reactors for hydrogenation and dehydrogenation processes based on supported palladium. J. Molec. Catal. A-Chem. 173 (2001) 135-184.

[18]. F. Gallucci, M. van Sint Annaland, J.A.M. Kuipers, Theoretical comparison of packed bed and fluidized bed membrane reactors for methane reforming. Int. J. Hydrogen Energy. 35 (2010) 7142-7150.

[19]. A. Mahecha-Botero, Z. Chen, J.R. Grace, S.S.E.H. Elnashaie, C.J. Lim, M. Rakib, I. Yasuda, Y. Shirasaki, Comparison of fluidized bed flow regimes for steam methane reforming in membrane reactors: A simulation study. Chem. Eng. Sci. 64 (2009) 3598-3613.

[20] T.Y.N. Dang, F. Gallucci, M. van Sint Annaland, Microstructured fluidized bed membrane reactors: solids circulation and densified zones distribution, Chem. Eng. J. 239 (2014) 42-52.

[21]. J. Wang, L. Tan, M.A. van der Hoef, M. van Sint Annaland, J.A.M. Kuipers, From bubbling to turbulent fluidization: advanced onset of regime transition in micro-fluidized beds. Chem. Eng. Sci. 66 (2011) 2001-2007.

[22]. M.A. van der Hoef, M. Ye, M. van Sint Annaland, A.T. Andrews, S. Sundaresan, J.A.M. Kuipers, Multiscale modeling of gas-fluidized beds. Adv. Chem. Eng. 31 (2006) 65-149.

[23]. N. Herzog, M. Schreiber, C. Egbers, H.J. Krautz. A comparative study of different CFD-codes for numerical simulation of gas-solid fluidized bed hydrodynamics. Comput. Chem. Eng. 39 (2012) 41-46.

[24]. A. Busciglio, G. Vella, G. Micale, L. Rizzuti, Analysis of the bubbling behaviour of 2D gas solid fluidized beds Part II. Comparison between experiments and numerical simulations via Digital Image Analysis Technique. Chem. Eng. J. 148 (2009) 145-163.

[25]. V.V. Ranade, Computational flow modelling for Chemical Reactor Engineering. Academic Press, London. 2002.

[26]. D.C. Sau, K.C. Biswal. Computational fluid dynamics and experimental study of the hydrodynamics of a gas–solid tapered fluidized bed. Appl. Math. Model. 35 (2011) 2265-2278.

[27]. W. Duangkhamchan, F. Ronsse, F. Depypere, K. Dewettinck, J.G. Pieters, Comparison and evaluation of interphase momentum exchange models for simulation of the solids volume fraction in tapered fluidised beds. Chem. Eng. Sci. 65 (2010) 3100-3112.

[28]. P. Pei, K. Zhang, J. Ren, D. Wen, G. Wu, CFD simulation of a gas–solid fluidized bed with two vertical jets. Particuology. 8 (2010) 425-432.

[29]. J.A. Medrano, R.J.W. Voncken, I. Roghair, F. Gallucci, M. van Sint Annaland, On the effect of gas pockets surrounding membranes in fluidized bed membrane reactors: An experimental and numerical study. Chem. Eng. J. In press. DOI: 10.1016/j.cej.2015.04.007

[30]. J.F. de Jong, T.Y.N. Dang, M. van Sint Annaland, J.A.M. Kuipers, Comparison of a Discrete Particle Model and a Two-Fluid Model to experiments of a fluidized bed with flat membranes. Powder Technol. 230 (2012) 93-105.

[31]. M.J.H. Khan, M.A. Hussain, Z. Mansourpour, N. Mostoufi, N.M. Ghasem, E.C. Abdullah, CFD simulation of fluidized bed reactors for polyolefin production – A review. J. Ind. Eng. Chem. 20 (2014) 3919-3946.

[32]. P. Lettieri, G. Saccone, L. Cammarata, Predicting the transition from bubbling to slugging fluidization using Computational Fluid Dynamics. Chem. Eng. Res. Design. 82 (2004) 939-944.

[33]. L. Cammarata, P. Lettieri, G.D.M. Micale, D. Colman, 2D and 3D CFD simulations of bubbling fluidized beds using Eulerian-Eulerian models. Int. J. Chem. React. Eng. 1 (2003) A48.

[34]. J.R. Grace, F. Taghipour, Verification and validation of CFD models and dynamic similarity for fluidized beds. Powder Technol. 139 (2004) 99-110.

[35]. W. Jeong, J. Seong, Comparison of effects on technical variances of computational fluid dynamics (CFD) software based on finite element and finite volume methods. Int. J. Mech. Sci. 78 (2014) 19-26.

[36]. G.H. Lee, Y.S. Bang, S.W. Woo, D.H. Kim, M.K. Kang, Comparative study of commercial CFD software performance for prediction of reactor internal flow. Transactions of the KSME, B. 37 (2013) 1175-1183.

[37]. C.K.K. Lun, S.B. Savage, The effects of an impact velocity dependent coefficient of restitution on stresses developed by sheared antigranulocytes-materials. Acta Mech. 63 (1986) 15-44.

[38]. D. Gidaspow, Multiphase flow and fluidization: continuum and Kinetic Theory descriptions. Academic Press, San Diego. 1994.

[39]. D.G. Schaeffer, Instability in the evolution equations describing incompressible granular flow. J. Diff. Eq. 66 (1987) 19-50.

[40]. S. Cloete, A. Zaabout, S.T. Johansen, M. van Sint Annaland, F. Gallucci, S. Amini, The generality of the standard 2D TFM approach in predicting bubbling fluidized bed hydrodynamics. Powder Technol. 235 (2013) 735-46.

[41]. C.K.K. Lun, S.B. Savage, D.J. Jeffrey, N. Chepurniy, Kinetic Theories for Granular Flow: Inelastic particles in couette flow and slightly inelastic particles in a general flow field. J. Fluid Mech. 140 (1984) 223-256.

[42]. G.N. Ahuja, A.W. Patwardhan, CFD and experimental studies of solids hold-up distribution and circulation patterns in gas–solid fluidized beds. Chem. Eng. J. 143 (2008) 147-160.

[43]. F. Hernández-Jiménez, A. Gómez-García, D. Santana, A. Acosta-Iborra, Gas interchange between bubble and emulsion phases in a 2D fluidized bed as revealed by two-fluid model simulations. Chem. Eng. J. 215–216 (2013) 479-490.

[44]. V. Verma, J.T. Padding, N.G. Deen, J.A.M. Kuipers, Bubble formation at a central orifice in a gas–solid fluidized bed predicted by three-dimensional two-fluid model simulations. Chem. Eng. J. 245 (2014) 217-227.

[45]. S. Cloete, S.T. Johansen, S. Amini, Investigation into the effect of simulating a 3D cylindrical fluidized bed reactor on a 2D plane. Powder Technol. 239 (2013) 21-35.

[46]. A. Bahramian, M. Olazar, G. Ahmadi, Effect of slip boundary conditions on the simulation of microparticle velocity fields in a conical fluidized bed. AIChE J. 59 (2013) 4502-4518.

[47]. T. Li, S. Benyahia, Evaluation of wall boundary condition parameters for gas-solids fluidized bed simulations. AIChE J. 59 (2013) 3624-3632.

[48]. T. Li, S. Benyahia, Revisiting Johnson and Jackson boundary conditions for granular flows. AIChE J. 58 (2012) 2058-2068.

[49]. S. Schneiderbauer, A. Aigner, S.A. Pirker, A comprehensive frictional-kinetic model for gas-particle flows: analysis of fluidized and moving bed regimes. Chem. Eng. Sci. 80 (2012) 279-292.

[50]. Y. Zhao, Y. Zhong, Y. He, H.I. Schlaberg, Boundary conditions for collisional granular flows of frictional and rotational particles at flat walls, AIChE J. 60 (2014) 4065-4075.

[51]. P.C. Johnson, R. Jackson, Frictional-collisional constitutive relations for granular materials, with application to plane shearing. J. Fluid Mech. 176 (1987) 67-93.

[52]. J.A. Medrano, I. Julián, J. Herguido, M. Menéndez, Pd-Ag membrane coupled to a Two-Zone Fluidized Bed Reactor (TZFBR) for propane dehydrogenation on a Pt-Sn/$MgAl_2O_4$ catalyst. Membranes. 3 (2013) 69-86.

[53]. D.J. Patil, M. van Sint Annaland, J.A.M. Kuipers, Critical comparison of hydrodynamic models for gas–solid fluidized beds—Part II: freely bubbling gas–solid fluidized beds. Chem. Eng. Sci. 60 (2005) 73-84.

[54]. T.W. Asegehegn, M. Schreiber, H.J. Krautz, Numerical simulation and experimental validation of bubble behavior in 2D gas-solid fluidized beds with immersed horizontal tubes. Chem. Eng. Sci. 66 (2011) 5410-5427.

[55]. R.P. Utikar, V.V. Ranade, Single jet fluidized beds: Experiments and CFD simulations with glass and polypropylene particles RID A-5627-2009. Chem. Eng. Sci. 62 (2007) 167-183.

[56]. J.A.M. Kuipers, K.J. van Duin, F.P.H. van Beckum, W.P.M. van Swaaij, Computer-simulation of the hydrodynamics of a 2-Dimensional gas-fluidized bed. Comput. Chem. Eng. 17 (1993) 839-858.

[57]. J.A.M. Kuipers, K.J. van Duin, F.P.H. van Beckum, W.P.M. van Swaaij, A numerical-model of gas-fluidized beds. Chem. Eng. Sci. 47 (1992) 1913-1924.

Table 1. TFM model parameters

Model parameter	Value
Reactor height (cm)	30
Solids density, ρ_s (kg/m^3)	2500
Particle size, d_p (μm)	200
Particles per cell unit, $d_p/cell$ (-)	≤ 6
Maximum bed packing, $\varepsilon_{s,m}$ (-)	0.65
Restitution coefficient, e (-)	0.95
Angle of internal friction, φ (^{o})	30
Gas temperature, T (^{o}C)	25

Table 2. Defluidization angle, β, as a function of gas velocity and membrane configuration

ITM	**u_r = 1.5**	**u_r = 2.5**
0%	74.1 ± 0.4	69.7 ± 0.1
20%	74.4 ± 0.3	73.2 ± 1.2
50%	76.9 ± 0.3	73.6 ± 1.1
RWM	**u_r = 1.5**	**u_r = 2.5**
0%	74.1 ± 0.4	69.7 ± 0.1
20%	81.7 ± 1.0	79.0 ± 2.5
50%	82.6 ± 0.1	81.5 ± 0.4

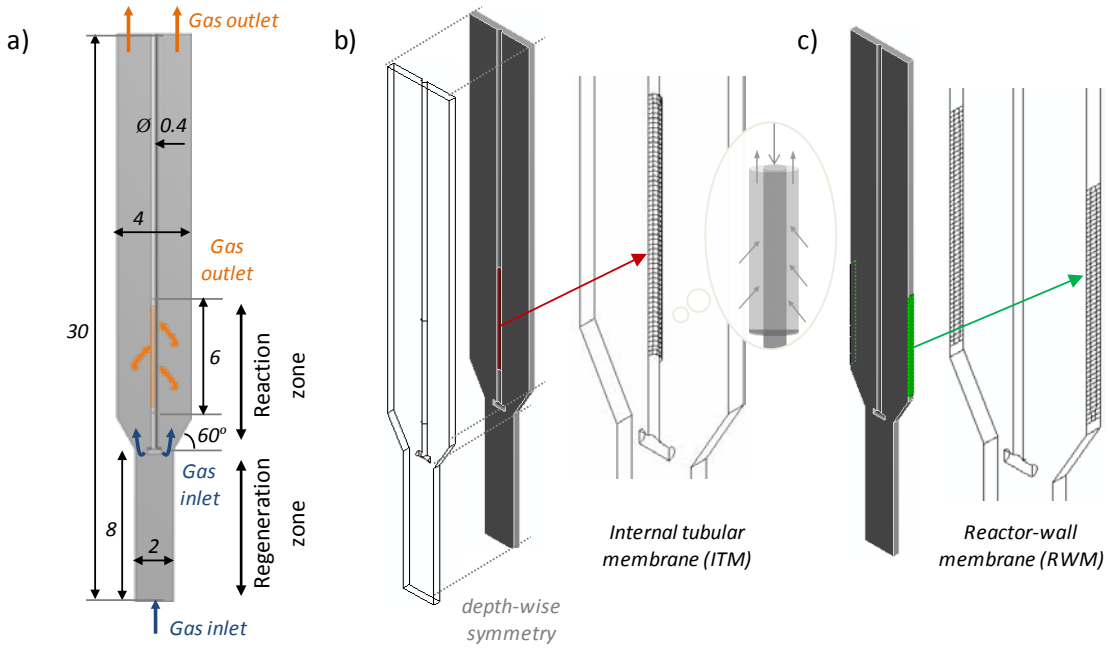

Figure 1. a) TS-TZFBR+M scheme, lengths in cm, b) ITM configuration, c) RWM configuration.

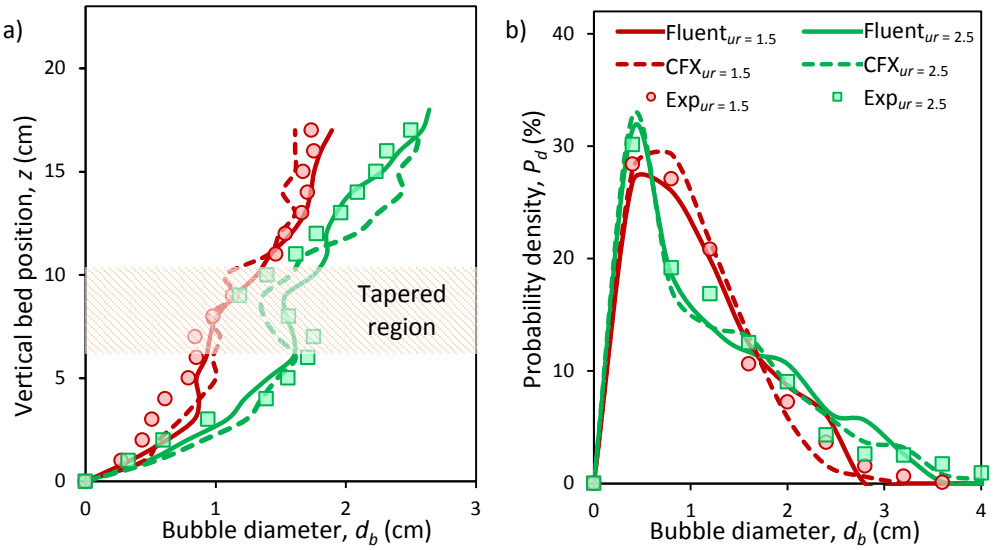

Figure 2. Comparison between experimental [6] and simulated (CFX and Fluent): a) axial equivalent bubble diameter profile, b) Bubble size distribution in a TS-TZFBR without gas extraction at relative gas velocities, u_r = 1.5 and 2.5.

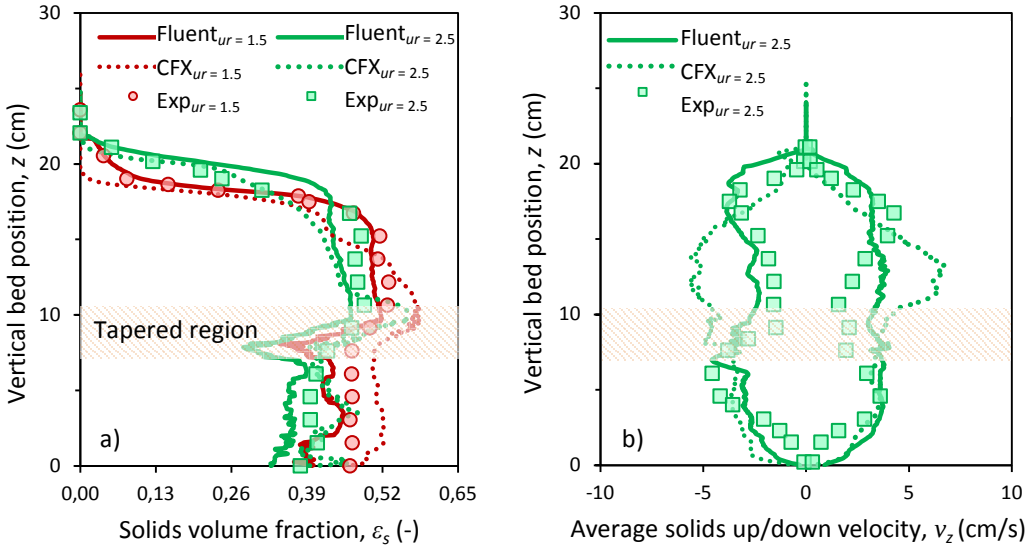

Figure 3. Comparison between experimental [6] and simulated (CFX and Fluent): a) solids hold-up in a TS-TZFBR without gas extraction at u_r = 1.5 and 2.5, b) upward and downward solids velocity at u_r = 2.5.

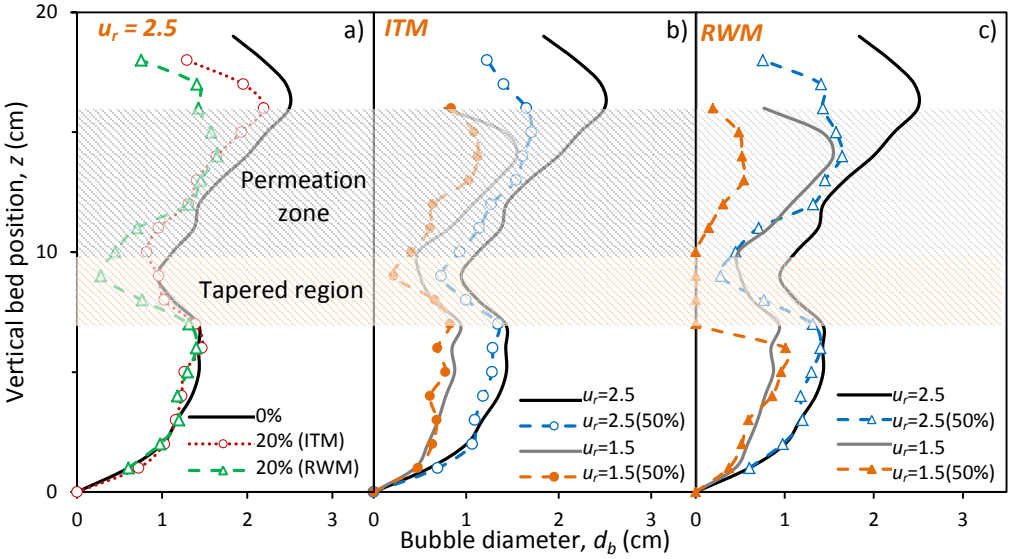

Figure 4. Axial evolution of the average equivalent bubble diameter. Effect of membrane configuration (a), gas velocity and permeation rate for tubular (b) and wall (c) membranes.

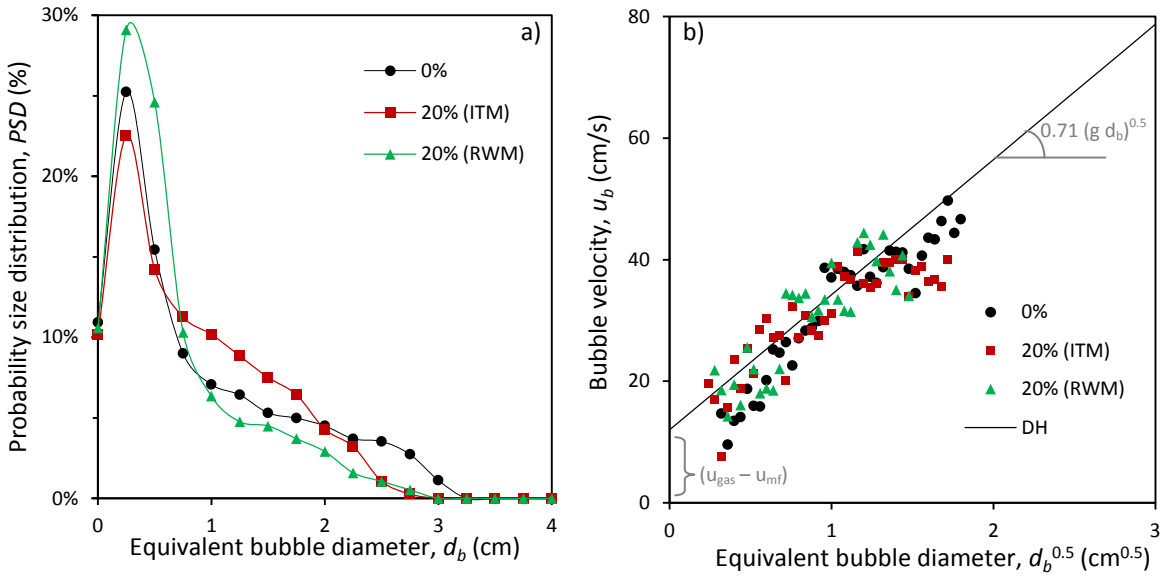

Figure 5. a) Simulated probability size distribution for different membrane-assisted TS-TZFBR configurations with and without gas extraction at u_r = 2.5. b) Time-averaged bubble velocity profiles for TS-TZFBR, TS-TZFBMR (ITM) and TS-TZFBMR (RWM) against the Davidson-Harrison $u_b(d_b^{0.5})$ correlation.

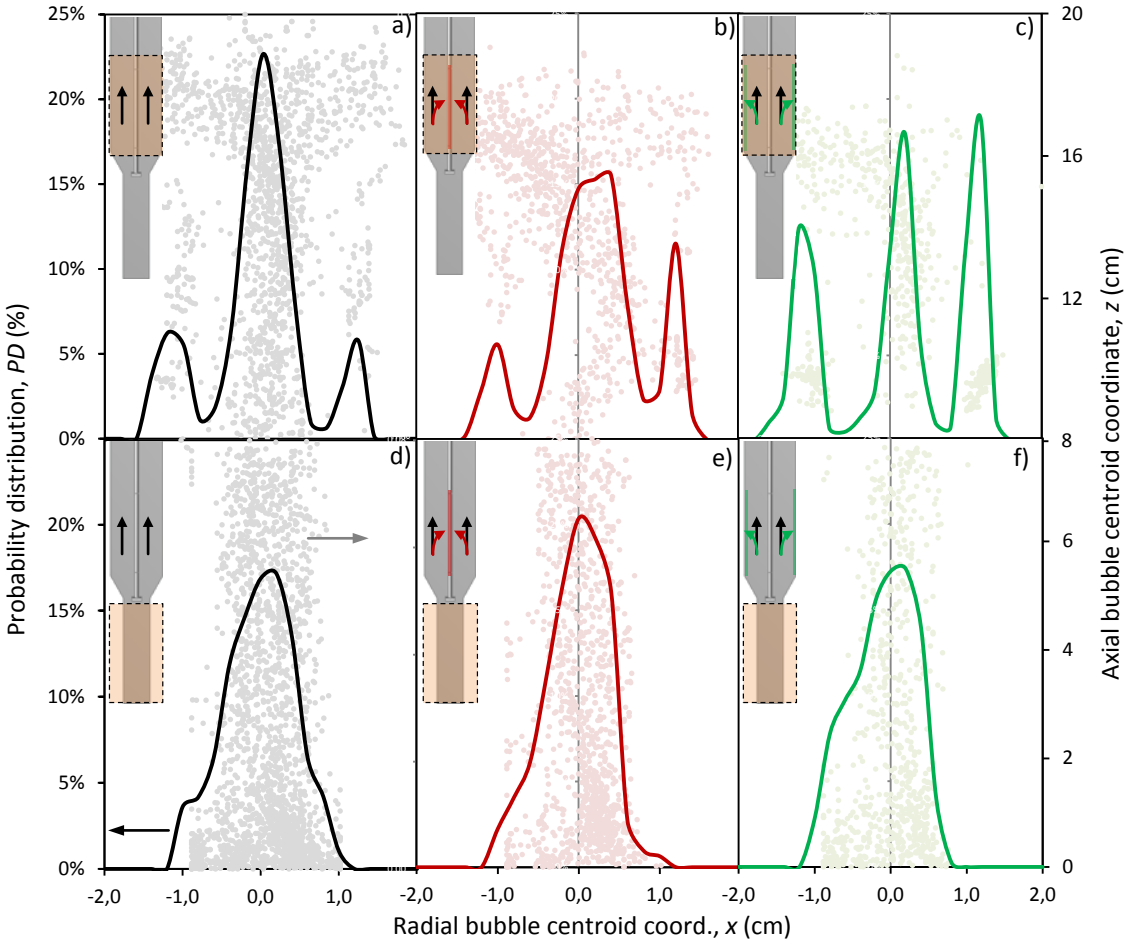

Figure 6. Effect of the membrane arrangement on the probability distribution of bubbles radial location within different bed regions: upper (a, b, c) and lower (d, e, f) bed zones for TS-TZFBR (a, d), TS-TZFBMR [ITM] (b, e) and TS-TZFBMR [RWM] (c, f). Fluidization regime: u_r = 2.5. Permeation rate: 20%.

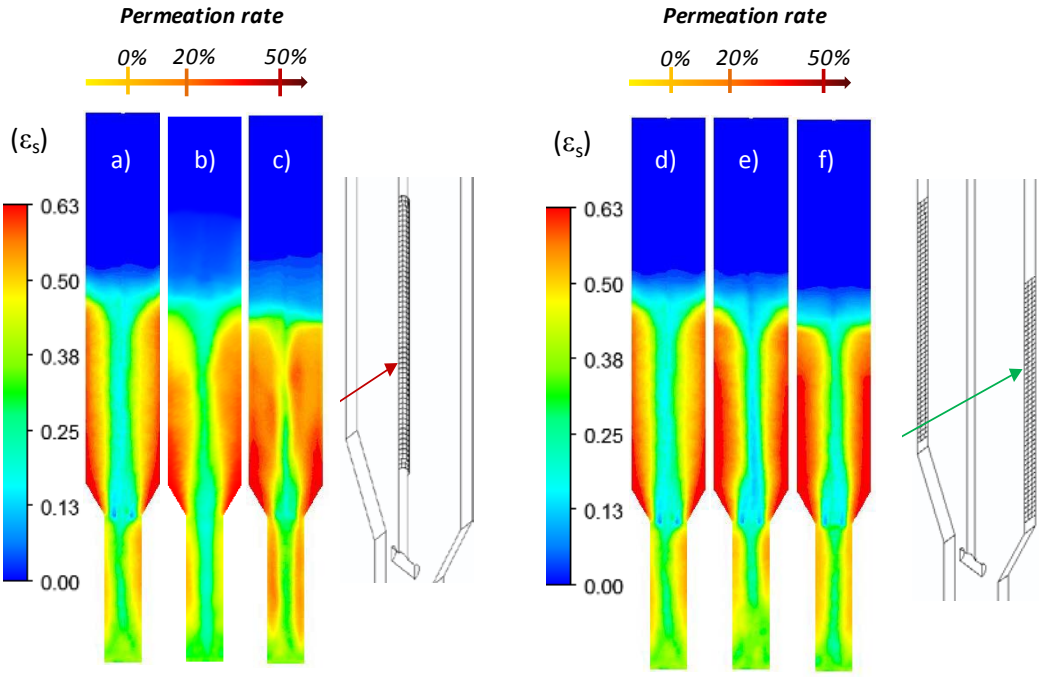

Figure 7. Time-averaged solids volume fraction (ε_s) distribution maps for ITM (a, b, c) and RWM (d, e, f) membrane-assisted TS-TZFBR configurations at bed depth y = 0.4 cm operated at 0%, 20% and 50% gas extraction rate, respectively. Inlet gas velocity: u_{gas}/u_{mf} = 2.5.

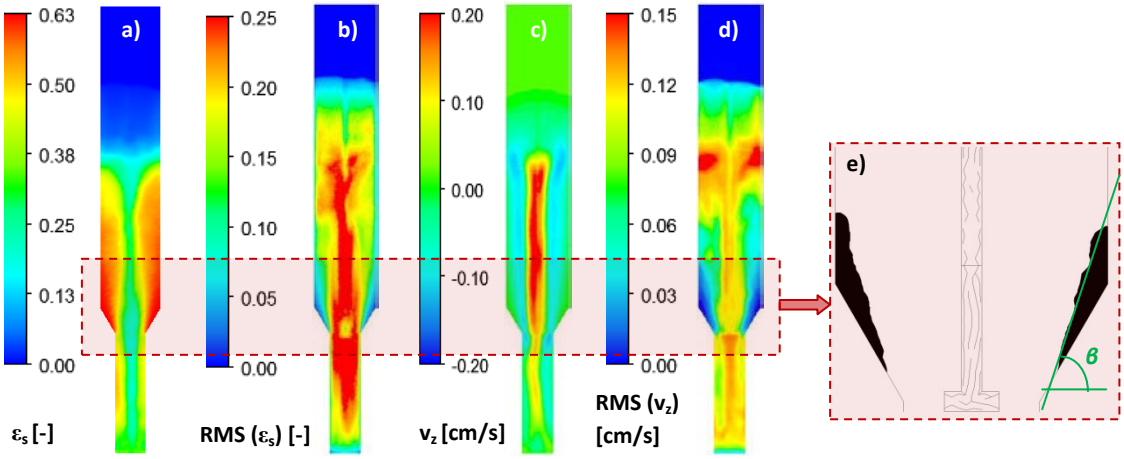

Figure 8. Time-averaged spatial distribution of: a) bed porosity, b) porosity fluctuation, c) axial solids velocity, d) axial velocity fluctuation, e) defluidized (or dead) bed regions. Operational conditions: TS-TZFBMR (ITM) at u_r = 2.5 and 20% permeation rate. Bed depth, y = 0.4 cm.